Measurement 224 (2024) 113935

Contents lists available at ScienceDirect

Measurement

journal homepage: www.elsevier.com/locate/measurement

Prediction and ephemeris fitting of LEO navigation satellites orbits computed at the antenna phase center

Kan Wang [a,b,*], Hang Su [a], Ahmed El-Mowafy [c], Xuhai Yang [a,b]

[a] National Time Service Center, Chinese Academy of Sciences, Xi'an, China
[b] University of Chinese Academy of Sciences, Beijing, China
[c] School of Earth and Planetary Sciences, Curtin University, Perth, Australia

ARTICLE INFO

Keywords:
Low Earth Orbit (LEO)
Antenna Phase Center (APC)
Precise Orbit Determination (POD)
Orbit prediction
Attitude control
Ephemeris fitting

ABSTRACT

Nowadays, Low Earth Orbit (LEO) satellites are proposed to augment the Positioning, Navigation and Timing (PNT) service of the GNSS satellites by directly transmitting navigation signals. In such cases, the users eventually need the orbits at the Antenna Phase Center (APC) of the antenna broadcasting navigation signals toward the Earth instead of those at the satellite Center of Mass (CoM). Using real attitudes of Sentinel satellites and simulated attitudes of different source types with enlarged instabilities, the influences of the attitude instability on the prediction and ephemeris fitting of the APC orbits are studied. It was found that different scenarios of attitude stabilities could lead to prediction degradations with a 3D RMS from a few millimeters to more than 4 cm. The study also showed that the ephemeris fitting errors of the APCs are not significantly impacted, considering both the real attitudes of Sentinel-6A and the simulated attitude instabilities.

1. Introduction

In recent years, low Earth orbit (LEO) satellites have been frequently discussed for the augmentation of the global navigation satellite systems (GNSSs) to provide resilient ground-based positioning, navigation, and timing (PNT) services [1–3]. The low altitudes of the LEO satellites, ranging from a few hundred kilometers to about 1500 km [4], have been demonstrated to improve the GNSS satellite Precise Orbit Determination (POD) by improving the satellite geometry [5]. In addition, they benefit PNT services directly when operating as navigation satellites. They provide signal strengths that are 30 dB stronger than those of the medium Earth orbits (MEO) GNSS satellites [6], and have a much faster speed (about 7 km/s). This offers a rapid geometry change and a significantly shortened convergence time of the precise point positioning (PPP) processing [7,8] and the PPP – real-time kinematic (PPP-RTK) positioning [2]. For such reasons, navigation-oriented LEO satellite constellations, such as Xona PULSAR [9] and CentiSpace [10], have been initiated. The latter launched two test satellites S3/S4 in September 2022 [11].

High-accuracy GNSS POD has been intensively investigated for decades [12–16]. To enable real-time PNT services, similar to the GNSS satellites, LEO satellite orbital products need to be provided to users with high precision in real-time. Compared to the GNSS satellites, the footprints of the LEO satellites are much smaller due to their much lower altitudes [17]. This leads to difficulties in determining continuous and high-precision orbits via the navigation signals from the LEO satellites to a network of ground stations [18] following the traditional GNSS POD strategies. For LEO satellites, a rather high density of ground stations is required, and gaps caused by the ocean and remote areas are difficult to be avoided [19,20]. Fortunately, LEO satellite orbits can be determined with high precision either in the kinematic mode using only the GNSS measurements or in the reduced-dynamic mode combining the GNSS measurements tracked onboard and dynamic models [21]. Mao et al. [22] reported a 1 cm POD accuracy in the post-processed ambiguity-fixed solution using dual-frequency GPS observations. A near-real-time POD accuracy from a few cm to around 1 dm can also be achieved using GPS measurements, depending on the accuracy of the used real-time GPS products [23,24]. Real-time GPS-based LEO POD were studied based on either a Kalman filter [25] or a batch least-squares adjustment followed by a short-term prediction [26], achieving a sub-dm to dm-level accuracy, depending on the strategies and the real-time GNSS products used. Multi-constellation GNSS measurements tracked onboard LEO satellites have also been studied in recent years for LEO POD [27–29]. For Sentinel-6A combining the GPS and Galileo

* Corresponding author at: National Time Service Center, Chinese Academy of Sciences, Xi'an, China.
E-mail address: wangkan@ntsc.ac.cn (K. Wang).

https://doi.org/10.1016/j.measurement.2023.113935
Received 15 July 2023; Received in revised form 8 November 2023; Accepted 24 November 2023
Available online 27 November 2023

observations, an accuracy of about 1 dm was reported for potential onboard real-time POD using the broadcast ephemeris [30], and an accuracy of about 7–9 cm was achieved using the Galileo high accuracy service (HAS) signals in simulated real-time processing [31].

While the inter-satellite links have nowadays made real-time data downlinking possible [32], the GNSS observations tracked onboard LEO satellites are expected to be transferred back to the ground in near-real-time rather than waiting for the next observation time window for the ground network. In such cases, near-real-time POD can be enabled on the ground with powerful processing units with various choices of high-precision real-time GNSS products that exhibit good accuracy. With a short processing time of a few minutes, one can benefit from the robustness and good data pre-processing capability of the batch least-squares adjustment for a single LEO POD. The real-time orbits can afterward be obtained by applying appropriate prediction strategies and fitting periods, LEO satellite orbits can be predicted in short-term, i.e., within half an hour, with good accuracies of a few cm, depending on the LEO satellite orbital heights, and then fit into LEO-specific ephemeris parameters [33,34].

The LEO satellite prediction and ephemeris fitting are, however, so far investigated for the LEO satellite center of mass (CoM), defined here as the CoM orbits. For future potential navigation users, it is more convenient to directly link the LEO satellite observations to the coordinates of the antenna phase center (APC), i.e., the APC orbits, transmitting the navigation signals toward the Earth. These coordinates are transmitted through ephemeris parameters, similar to the broadcast ephemeris of the GNSS satellites [35].

The APC ephemeris parameters of LEO satellites are, however, different from those of the GNSS broadcast ephemeris in the following aspects:

- For GNSS satellites, to obtain high-precision GNSS satellite orbits and clocks, corrections to the broadcast ephemeris are delivered to users through real-time streams by various analysis centers. The broadcast GNSS ephemeris usually exhibit a lower precision, i.e., generally at a few dm to meter level, depending on the satellite constellations [36]. On the other hand, in this study, LEO ephemeris parameters are designed to be directly fitted using high-precision real-time LEO satellite APC orbits with similarly high accuracy, i.e., at a few cm.
- LEO satellites are mostly of much lower cost compared to the GNSS satellites, and thus could suffer from using less stable attitude control systems. While the real-time attitude data can be tracked onboard and transmitted to the ground, aiding the precise APC determination, the prediction of APCs lacks attitude information and highly relies on attitude control. As the ephemeris parameters are generated based on the predicted APC orbits, the attitude control could also indirectly influence the ephemeris fitting errors.

In this study, for the first time, the prediction and ephemeris fitting of the LEO satellite APC orbits are investigated, considering the stability of the available LEO satellites attitude control. As real LEO-dedicated navigation satellites are not yet available for this study, the Sentinel-6A LEO satellite, which receives dual-frequency GPS and Galileo signals, is used for demonstration purposes. The CoM orbits are predicted in the short term and then adjusted to refer to the APC orbits. As shown in Fig. 1, the coordinate origin of the body-fixed system is the CoM. The satellite body-fixed system in practice (shown in blue as an example) could slightly vary from its expectation (shown in red), as even for science-oriented LEO satellites, the available attitude control is not perfect. The precise correction from the CoM to the APC thus needs precise attitude information. Due to the lack of attitude information during the prediction interval, the attitudes are predicted to correct the orbits from the CoM to the APC. For testing purposes, real attitudes of Sentinel-6A and other attitude scenarios with enlarged instabilities are simulated. The resulting degradations in the predicted APC orbits caused by the attitude prediction, and the corresponding degradations in the ephemeris fitting, are analyzed. The results would also inversely suggest the expected attitude stability when these degradations are expected to be limited within a certain level. Note that the body-fixed system could vary for different LEO satellites, and even for the same LEO satellites in different periods with the x-axis in or against the flight direction (e.g., the GRACE satellites). While the coordinate frame in Fig. 1 is illustrated for Sentinel-6A, for Sentinel-3B used also for testing in this contribution, the X-axis of the body-fixed system is expected to point in the opposite direction to the along-track direction.

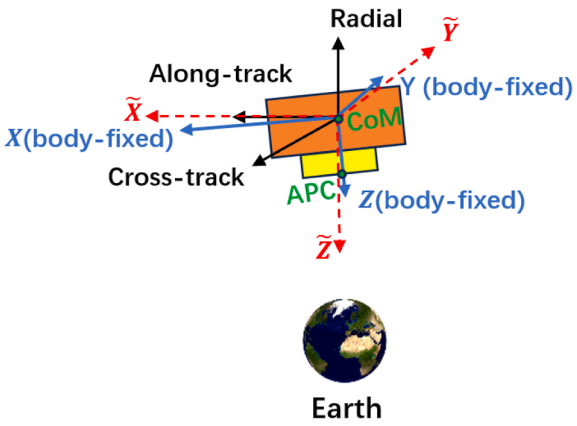

Fig. 1. Different coordinate frames of Sentinel-6A as an example LEO satellite.

In the following sections, the strategy to predict the orbital corrections from CoM to APC within 1 h is first introduced. Based on the real attitudes of Sentinel-6A and Sentinel-3B, different attitude instabilities are simulated to enlarge the potential attitude instabilities and check their influences on the corrections. With the lack of attitude data in the prediction interval, the attitude needed to be predicted. The resulting degradations in the predicted APC orbits and ephemeris fitting errors due to the attitude instabilities are analyzed. Finally, the discussions and conclusions are given at the end.

2. Processing strategy for APC orbit prediction and ephemeris fitting

Before the orbit prediction, the reduced-dynamic POD of LEO at its CoM needs to be performed by combining the GNSS phase and code observations tracked onboard with proper dynamic models. The CoM POD results are next predicted over a short term, e.g., 1 h in this study, resulting in the predicted CoM orbits. This process has been described in various studies [26,33] and thus is not the focus of this study. As such, it will not be described in this section again. Instead, this section focuses on attitude estimation in the orbit prediction interval.

2.1. Rotation angles between default and real attitudes

For satellites aiming to transmit navigation signals toward the Earth, the attitude is needed to allow the transmitter to steadily point towards the Earth. With R, T, A representing the radial, along-track and cross-track directions, the expected body-fixed frame is typically described in the following two cases:

A. X-axis in the along-track direction (T), Y-axis pointing in the opposite direction to the cross-track direction (-A), and Z-axis in the nadir direction (-R);
B. X-axis pointing in the opposite direction to the along-track direction (-T), Y-axis in the cross-track direction (A), and Z-axis in the nadir direction (-R).

The transformation matrix from the expected satellite body-fixed frame to the RTA frame can be expressed as:

$$R_{\mathrm{B2Bf}} = \begin{pmatrix} 0 & 0 & -1 \\ \delta & 0 & 0 \\ 0 & -\delta & 0 \end{pmatrix} \tag{1}$$

with $\delta = 1$ for case A, and $\delta = -1$ for case B.

In practice, the attitudes of the satellite do not behave perfectly as expected. As such, after multiplying the real body-fixed frame (i.e., the body-fixed frame in practice) by the rotation matrix R_{B2Bf}, slight differences would exist between the transformed body-fixed frame and the RTA frame. The matrix R_{RTA2Bf} that describes the rotation from the RTA frame to the transformed body-fixed frame is expressed as:

$$R_{\mathrm{RTA2Bf}} = R_{\mathrm{B2Bf}} R_{\mathrm{B2RTA}}^{\mathrm{T}} \tag{2}$$

where R_{B2RTA} is the transformation matrix from the real body-fixed frame to the RTA frame, which needs to be computed based on available attitude information and other Earth rotation information, as described below.

Using the possible attitude information generated onboard LEO satellites, it is possible to compute the transformation matrix R_{B2ECI} from the real body-fixed frame to the Earth-Centered Inertial (ECI) system, more specifically, J2000.0 [37]:

$$R_{\mathrm{B2ECI}} = \begin{pmatrix} 1 - 2 \times \left(q_2^2 + q_3^2\right) & 2 \times (q_1 q_2 - q_0 q_3) & 2 \times (q_1 q_3 + q_0 q_2) \\ 2 \times (q_1 q_2 + q_0 q_3) & 1 - 2 \times \left(q_1^2 + q_3^2\right) & 2 \times (q_2 q_3 - q_0 q_1) \\ 2 \times (q_1 q_3 - q_0 q_2) & 2 \times (q_2 q_3 + q_0 q_1) & 1 - 2 \times \left(q_1^2 + q_2^2\right) \end{pmatrix} \tag{3}$$

where q_0, q_1, q_2, q_3 are quaternion elements. It can be further transformed to the Earth-Centered Earth-Fixed (ECEF) system, and then to the RTA frame as follows:

$$R_{\mathrm{B2RTA}} = R_{\mathrm{ECEF2RTA}} R_{\mathrm{ECI2ECEF}} R_{\mathrm{B2ECI}} \tag{4}$$

where the transformation matrix from the ECI to the ECEF, i.e., R_{ECI2ECEF}, is related to the Earth rotation, the precession, the nutation, and the polar motions. The transformation matrix from the ECEF to the RTA frame (R_{ECEF2RTA}) can be formulated based on the LEO satellite CoM positions $\vec{r}_{\mathrm{L}}$ and velocities $\vec{v}_{\mathrm{L}}$ in the ECEF system in two ways, i.e., with respect to the satellite positions (see Eq. (5)), and with respect to the satellite velocities (Eq. (6)):

$$R_{\mathrm{ECEF2RTA}} = \begin{pmatrix} \dfrac{\vec{r}_{\mathrm{L}}}{\|\vec{r}_{\mathrm{L}}\|} \left(\dfrac{\vec{r}_{\mathrm{L}}}{\|\vec{r}_{\mathrm{L}}\|} \times \dfrac{\vec{v}_{\mathrm{L}}}{\|\vec{v}_{\mathrm{L}}\|} \right) \times \dfrac{\vec{r}_{\mathrm{L}}}{\|\vec{r}_{\mathrm{L}}\|} \dfrac{\vec{r}_{\mathrm{L}}}{\|\vec{r}_{\mathrm{L}}\|} \times \dfrac{\vec{v}_{\mathrm{L}}}{\|\vec{v}_{\mathrm{L}}\|} \end{pmatrix} \tag{5}$$

$$R_{\mathrm{ECEF2RTA}} = \begin{pmatrix} \dfrac{\vec{v}_{\mathrm{L}}}{\|\vec{v}_{\mathrm{L}}\|} \times \left(\dfrac{\vec{r}_{\mathrm{L}}}{\|\vec{r}_{\mathrm{L}}\|} \times \dfrac{\vec{v}_{\mathrm{L}}}{\|\vec{v}_{\mathrm{L}}\|} \right) \dfrac{\vec{v}_{\mathrm{L}}}{\|\vec{v}_{\mathrm{L}}\|} \dfrac{\vec{r}_{\mathrm{L}}}{\|\vec{r}_{\mathrm{L}}\|} \times \dfrac{\vec{v}_{\mathrm{L}}}{\|\vec{v}_{\mathrm{L}}\|} \end{pmatrix} \tag{6}$$

As the position vector $\vec{r}_{\mathrm{L}}$ and velocity vector $\vec{v}_{\mathrm{L}}$ are almost perpendicular to each other for the near-circular LEO satellite orbits, the R_{ECEF2RTA} calculated with Eqs. (5) and (6) do not differ much. In this study, the R_{ECEF2RTA} computed with respect to the satellite velocities (Eq. (6)) is used.

With R_{B2RTA} calculated according to Eq. (4), the matrix R_{RTA2Bf} (Eq. (2)) rotating over small angles between the RTA frame and the transformed body-fixed frame can be computed. Assuming that the rotation matrix R_{RTA2Bf} can be described with the rotation by angle α_{X} around the X-axis, followed by the rotation by angle α_{Y} around the Y-axis, followed by the rotation by angle α_{Z} around the Z-axis, it can be formulated as:

$$R_{\mathrm{RTA2Bf}} = R_{\mathrm{X}}(\alpha_{\mathrm{X}}) R_{\mathrm{Y}}(\alpha_{\mathrm{Y}}) R_{\mathrm{Z}}(\alpha_{\mathrm{Z}})$$

$$= \begin{pmatrix} 1 & 0 & 0 \\ 0 & \cos(\alpha_{\mathrm{X}}) & \sin(\alpha_{\mathrm{X}}) \\ 0 & -\sin(\alpha_{\mathrm{X}}) & \cos(\alpha_{\mathrm{X}}) \end{pmatrix} \begin{pmatrix} \cos(\alpha_{\mathrm{Y}}) & 0 & \sin(\alpha_{\mathrm{Y}}) \\ 0 & 1 & 0 \\ -\sin(\alpha_{\mathrm{Y}}) & 0 & \cos(\alpha_{\mathrm{Y}}) \end{pmatrix} \begin{pmatrix} \cos(\alpha_{\mathrm{Z}}) & \sin(\alpha_{\mathrm{Z}}) & 0 \\ -\sin(\alpha_{\mathrm{Z}}) & \cos(\alpha_{\mathrm{Z}}) & 0 \\ 0 & 0 & 1 \end{pmatrix}$$

$$= \begin{pmatrix} \cos(\alpha_{\mathrm{Y}})\cos(\alpha_{\mathrm{Z}}) & \cos(\alpha_{\mathrm{Y}})\sin(\alpha_{\mathrm{Z}}) & \sin(\alpha_{\mathrm{Y}}) \\ -\sin(\alpha_{\mathrm{X}})\sin(\alpha_{\mathrm{Y}})\cos(\alpha_{\mathrm{Z}}) - \cos(\alpha_{\mathrm{X}})\sin(\alpha_{\mathrm{Z}}) & -\sin(\alpha_{\mathrm{X}})\sin(\alpha_{\mathrm{Y}})\sin(\alpha_{\mathrm{Z}}) + \cos(\alpha_{\mathrm{X}})\cos(\alpha_{\mathrm{Z}}) & \sin(\alpha_{\mathrm{X}})\cos(\alpha_{\mathrm{Y}}) \\ -\sin(\alpha_{\mathrm{Y}})\cos(\alpha_{\mathrm{X}})\cos(\alpha_{\mathrm{Z}}) + \sin(\alpha_{\mathrm{X}})\sin(\alpha_{\mathrm{Z}}) & -\sin(\alpha_{\mathrm{Y}})\cos(\alpha_{\mathrm{X}})\sin(\alpha_{\mathrm{Z}}) - \sin(\alpha_{\mathrm{X}})\cos(\alpha_{\mathrm{Z}}) & \cos(\alpha_{\mathrm{X}})\cos(\alpha_{\mathrm{Y}}) \end{pmatrix} \tag{7}$$

In such a case, the rotation angles α_{X}, α_{Y} and α_{Z} can be calculated as follows:

$$\alpha_{\mathrm{X}} = \arctan\left(\frac{R_{\mathrm{RTA2Bf}}(2,3)}{R_{\mathrm{RTA2Bf}}(3,3)} \right) \tag{8}$$

$$\alpha_{\mathrm{Y}} = \arctan\left(\frac{R_{\mathrm{RTA2Bf}}(1,3)}{\sqrt{R^2_{\mathrm{RTA2Bf}}(1,1)+R^2_{\mathrm{RTA2Bf}}(1,2)}}\right) \tag{9}$$

$$\alpha_{\mathrm{Z}} = \arctan\left(\frac{R_{\mathrm{RTA2Bf}}(1,2)}{R_{\mathrm{RTA2Bf}}(1,1)}\right) \tag{10}$$

where $R_{\mathrm{RTA2Bf}}(m,n)$ represents the element at the m^{th} row and the n^{th} column in the rotation matrix R_{RTA2Bf}.

2.2. Constructing the transformation matrix from the body-fixed frame to the ECEF system for APC orbit prediction

As mentioned in the last sub-section, the rotation angles between the transformed body-fixed frame and the RTA frame can be computed as long as the attitude data, i.e., the quaternions, are available. To predict the APC orbits (i.e. the orbits referenced to the APC), the matrix R_{RTA2Bf} needs to be re-constructed at each prediction epoch t_i, which requires the rotation angles $\alpha_{\mathrm{X}}(t_i)$, $\alpha_{\mathrm{Y}}(t_i)$ and $\alpha_{\mathrm{Z}}(t_i)$ to be predicted at the corresponding prediction epoch. In this study, for unknown patterns of attitude instabilities, it is assumed that the predicted rotation angles $\widehat{\alpha}_{\mathrm{X}}(t_i)$, $\widehat{\alpha}_{\mathrm{Y}}(t_i)$ and $\widehat{\alpha}_{\mathrm{Z}}(t_i)$ are equal to the latest rotation angles in the POD interval, denoted as $\alpha_{\mathrm{X}}(t_0)$, $\alpha_{\mathrm{Y}}(t_0)$ and $\alpha_{\mathrm{Z}}(t_0)$. They can be expressed as:

$$\widehat{\alpha}_{\mathrm{X}}(t_i) = \alpha_{\mathrm{X}}(t_0), \widehat{\alpha}_{\mathrm{Y}}(t_i) = \alpha_{\mathrm{Y}}(t_0), \widehat{\alpha}_{\mathrm{Z}}(t_i) = \alpha_{\mathrm{Z}}(t_0) \tag{11}$$

where $\alpha_{\mathrm{X}}(t_0)$, $\alpha_{\mathrm{Y}}(t_0)$ and $\alpha_{\mathrm{Z}}(t_0)$, are assumed known. The differences between the predicted and real rotation angles at t_i would then lead to degradations when correcting the orbits from CoM to the APC.

With the predicted $\widehat{\alpha}_{\mathrm{X}}(t_i)$, $\widehat{\alpha}_{\mathrm{Y}}(t_i)$ and $\widehat{\alpha}_{\mathrm{Z}}(t_i)$, the matrix R_{RTA2Bf} at the prediction epoch t_i can be re-constructed according to Eq. (7) as:

$$R_{\mathrm{RTA2Bf}}(t_i) = R_{\mathrm{X}}(\widehat{\alpha}_{\mathrm{X}}(t_i))R_{\mathrm{Y}}(\widehat{\alpha}_{\mathrm{Y}}(t_i))R_{\mathrm{Z}}(\widehat{\alpha}_{\mathrm{Z}}(t_i)) \tag{12}$$

The re-constructed matrix $R_{\mathrm{RTA2Bf}}(t_i)$ helps to form the transformation matrix from the real body-fixed frame to the ECEF system at the prediction epoch t_i with:

$$R_{\mathrm{B2ECEF}}(t_i) = R^{\mathrm{T}}_{\mathrm{ECEF2RTA}}(t_i)R^{\mathrm{T}}_{\mathrm{RTA2Bf}}(t_i)R_{\mathrm{B2Bf}} \tag{13}$$

where the matrix R_{ECEF2RTA} at the prediction epoch t_i can be computed according to Eq. (6) using the predicted orbits $\overrightarrow{r}_{\mathrm{L}}(t_i)$ and velocities $\overrightarrow{v}_{\mathrm{L}}(t_i)$ in the ECEF system.

2.3. Correction of the predicted CoM orbits to APC orbits

Assuming that the vector from the LEO satellite orbits presented at its CoM to the APC is known in the body-fixed frame based on calibrations on the ground or in-flight, the vector can be transformed to the ECEF system using the $R_{\mathrm{B2ECEF}}(t_i)$ in Eq. (13) at the prediction epoch t_i:

$$\Delta\overrightarrow{\gamma}_{\mathrm{LE}}(t_i) = R_{\mathrm{B2ECEF}}(t_i)\Delta\overrightarrow{\gamma}_{\mathrm{LB}} \tag{14}$$

where $\Delta\overrightarrow{\gamma}_{\mathrm{LB}}$ represents the vector from the CoM to the APC in the body-fixed frame, and $\Delta\overrightarrow{\gamma}_{\mathrm{LE}}(t_i)$ denotes its counterparts in the ECEF system at the prediction epoch t_i.

With the $\Delta\overrightarrow{\gamma}_{\mathrm{LE}}(t_i)$ calculated, it is possible to correct the predicted CoM orbits ($\overrightarrow{r}_{\mathrm{L}}(t_i)$) into the predicted APC orbits ($\overrightarrow{r}_{\mathrm{L,APC}}(t_i)$) as follows:

$$\overrightarrow{r}_{\mathrm{L,APC}}(t_i) = \overrightarrow{r}_{\mathrm{L}}(t_i) + \Delta\overrightarrow{\gamma}_{\mathrm{LE}}(t_i) \tag{15}$$

2.4. Ephemeris fitting of the predicted APC orbits

Using the predicted APC orbits $\overrightarrow{r}_{\mathrm{L,APC}}(t_i)$, with a proper set of ephemeris parameters and fitting time selected, the APC orbits can be fitted into ephemeris parameters with a good precision. To well describe the near-circular LEO satellite orbits with an eccentricity $e \approx 0$, the traditional GNSS-like ephemeris parameters need to be re-formed to avoid the near-singularity between the mean anomaly M and the argument of perigee ω [38]. In general, the number of ephemeris parameters, the length of the fitting interval, and the LEO satellite orbital heights commonly influence the ephemeris fitting errors [26,38].

In this study, the focus is put on the enlarged ephemeris fitting errors of the APC orbits compared to the CoM orbits due to the APC prediction. For example, the tests are performed for 18-parameter ephemeris fitting of Sentinel-6A at around 1300 km with a fitting time of 10 min. The 18 parameters used for the orbit fitting are listed in Table 1. Note that e_x, e_y and γ_0 need to be transformed back to e, ω and M_0 after the fitting.

3. Test results

This section is split into three parts. Firstly, taking the POD solutions of the Sentinel-6A as a representative LEO satellite example, it briefly introduces the accuracy of the near-real-time POD and the short-term prediction that can be achieved nowadays for LEO satellites at relatively high altitudes, i.e., around 1300 km. Next, using real attitudes of Sentinel-6A and different simulated attitude scenarios, the degradations in the predicted APC orbits caused by the attitude instabilities are evaluated. Finally, compared to the CoM ephemeris fitting, the errors of fitting the APC orbits are assessed for real attitudes of Sentinel-6A and different simulated attitude scenarios.

3.1. Multi-GNSS near-real-time POD and prediction of the CoM

Sentinel-6A receives GPS observations on L1/L2 and Galileo observations on E1/E5a. The tracking channels for Galileo observations are E1C and E5aQ, while the channels used for the GPS processing are L1C or L1W for L1, and L2L or L2W for L2. The CoM orbits of Sentinel-6A are processed within 24 h with a sampling interval of 30 s in the reduced-dynamic mode with a batch least-squares adjustment using the real-time GNSS satellite clock and orbital products from the National Center for Space Studies (CNES) real-time service (RTS). The data from February 1 to 7, 2022, were used for processing. The estimated and predicted orbits of the LEO satellite Sentinel-6A are compared with the

Table 1
The 18 estimable ephemeris parameters used for fitting the LEO satellite APC orbits.

Estimable ephemeris parameters	Explanation
t_e	Reference time
e_x, e_y	$e_x = e\times\cos(\omega)$, $e_y = e\times\sin(\omega)$
γ_0	$\gamma_0 = \omega + M_0$
a	Semi-major axis
I_0	Inclination at the reference time
Ω_0	Right Ascension of Ascending Node (RAAN) at the reference time
Δn	Mean motion correction
$\dot{I}$, $\dot{\Omega}$	Rate of the inclination and the RAAN
$Cus2$, $Cuc2$, $Crs2$, $Crc2$, $Cis2$, $Cic2$	Second-order harmonic coefficients
$\dot{a}$, $\dot{n}$	Rate of the semi-major axis and the mean motion

Table 2
The accuracies for different CoM orbit solutions of Sentinel-6A in the GPS + Galileo combined case using the CNES RTS products.

Solution type	σ_{R} (m)	σ_{T} (m)	σ_{A} (m)	σ_{3D} (m)	σ_{OURE} (m)
POD	0.011	0.019	0.018	0.028	0.016
Prediction at 5 min	0.018	0.036	0.021	0.045	0.025
Prediction at 10 min	0.017	0.041	0.022	0.049	0.027
Prediction at 15 min	0.017	0.046	0.022	0.053	0.030
Prediction at 20 min	0.017	0.049	0.023	0.057	0.032
Prediction at 30 min	0.017	0.059	0.024	0.066	0.036
Prediction at 1 h	0.020	0.080	0.025	0.086	0.047

reference orbits provided by the Copernicus POD service, which are processed in the ambiguity-fixed post-processing mode and exhibit a 3D RMSE of about 1 cm [28,39].

To assess the POD and the prediction accuracy, the starting time of each 24 h POD interval was shifted by 5 min, resulting in more than 1700 samples of the 24 POD processing rounds over the test days from February 1 to 6, 2022, for the POD, and the prediction is performed during the period from February 2 to 7, 2022, after each 24 h POD processing. For the prediction period of 1 h in this study, a fitting time of 4 h, i.e., the last 4 h in the POD processing time, is used to fit the orbital dynamic parameters, including the six Keplerian elements, the constant, sine and cosine terms of the solar radiation pressure (SRP) parameters [33,40]. In addition to the errors in the radial, along-track and cross-track directions, the 3D orbital errors and the orbital user range errors (OUREs) are assessed. The OURE can be considered as the projection of the orbital errors along the satellite-to-Earth direction (user location) in a global averaged sense. Its RMS, denoted as σ_{OURE}, can be expressed as:

$$\sigma_{\mathrm{OURE}} = \sqrt{\omega_{\mathrm{R}}^2\sigma_{\mathrm{R}}^2 + \omega_{\mathrm{TA}}^2(\sigma_{\mathrm{T}}^2 + \sigma_{\mathrm{A}}^2)} \tag{16}$$

where σ_{R}, σ_{T} and σ_{A} represents the RMS of the radial, along-track and cross-track orbital errors. The coefficients ω_{R} and ω_{TA} are determined based on the orbital height [41], which is estimated as 0.6398 and 0.5433, respectively, for Sentinel-6A with an orbital height of around 1346 km during the test week.

Table 2 summarizes the corresponding RMS for the whole testing period of the CoM POD orbits and the predicted CoM orbits at different prediction times in the radial (σ_{R}), along-track (σ_{T}) and cross-track (σ_{A}) directions. The 3D RMS (σ_{3D}) and the RMS of the OURE (σ_{OURE}) are given in the last two columns. By calculating the RMS, outliers outside the mean values ±4.42 times the corresponding standard deviations are excluded. As observed from Table 2, using high-precision real-time GNSS products nowadays, one can achieve a rather good POD accuracy with an OURE below 2 cm and a 3D RMS around 3 cm in near-real-time. The 3D RMSE and σ_{OURE} up to 1 hr prediction time are less than 9 cm and 5 cm, respectively.

3.2. Attitude stability and APC orbit prediction

As mentioned in Section 2, the attitude stability will influence the orbit correction from CoM to APC in the prediction interval, which lacks real attitude quaternions. In this section, the attitude stability of Sentinel-6A is evaluated, and a few other scenarios of attitude instabilities are simulated. The degradations in the predicted APC orbits due to the loss of attitude information are then analyzed under different attitude scenarios.

3.2.1. Attitude stability

Using the reference orbits and velocities provided by the Copernicus POD service, the left panel of Fig. 2 shows the three rotation angles between the transformed body-fixed frame and the RTA frame computed from the presented method (see Eqs. (7)–(10)) for Sentinel-6A on February 1, 2022. It can be seen that the attitudes of Sentinel-6A follow well the expectation (see Case A in Section 2.1) on the test day, i.e., the rotation angles are all within ± 0.2 degrees. The variation in the rotation angles exhibits periodic patterns, which can be verified from analysing their Fast Fourier Transformation (FFT) plot (see the right panel of Fig. 2). The definition of the rotation angles α_{X}, α_{Y} and α_{Z} are given before Eq. (7). From the right panel of Fig. 2, it can be seen that all three angles have once-per-revolution (1/rev) periodic effects, and angle α_{Z} is dominated by a twice-per-revolution (2/rev) pattern. The RMS of the three rotation angles and the corresponding variation rates of the angles are given in Table 3. It can be seen that for both tested Sentinel satellites, the rotation angles have an RMS around or below 0.1 degrees, and the RMS of the angle rates are generally between 0.0001 and 0.0002 degrees per second.

Taking the attitudes of LEO satellite Sentinel-3B as another example, the left panel of Fig. 3 shows its three rotation angles between the transformed body-fixed frame and the RTA frame on August 15, 2018. Clear 1/rev and 2/rev patterns can also be observed in the FFT plot (shown on the right panel of Fig. 3). As depicted in Table 3, the RMS of the rotation angles of Sentinel-3B are generally at the same level as those of Sentinel-6A, i.e., around or below 0.1 degrees. The angle rates have an RMS of around 0.0001–0.00025 degrees per second. In the right panel of Fig. 3, a small peak exists for α_X (blue) in addition to the dominant peaks for α_Y (red) and α_Z (green), similar to the case of Sentinel-6A.

To consider situations of a less stable attitude control than those of the two tested Sentinel satellites, scenarios A to F are tested with the three rotation angles simulated with different performances. Scenarios A to C contain 1/rev periodic patterns for all three rotation angles and 2/rev periodic patterns additionally for α_{Z}, while scenarios D to F have the rotation angles simulated as random-walk processes. More specifically, the rotation angles in Scenarios A to C are simulated as follows considering the periodic patterns shown in the Figs. 2 and 3:

$$\alpha_X = \Delta\alpha_X + A_S \times \sin\left(\frac{2\pi}{T} \times t\right) \tag{17}$$

$$\alpha_Y = \Delta\alpha_Y + A_S \times \sin\left(\frac{\pi}{3} + \frac{2\pi}{T} \times t\right) \tag{18}$$

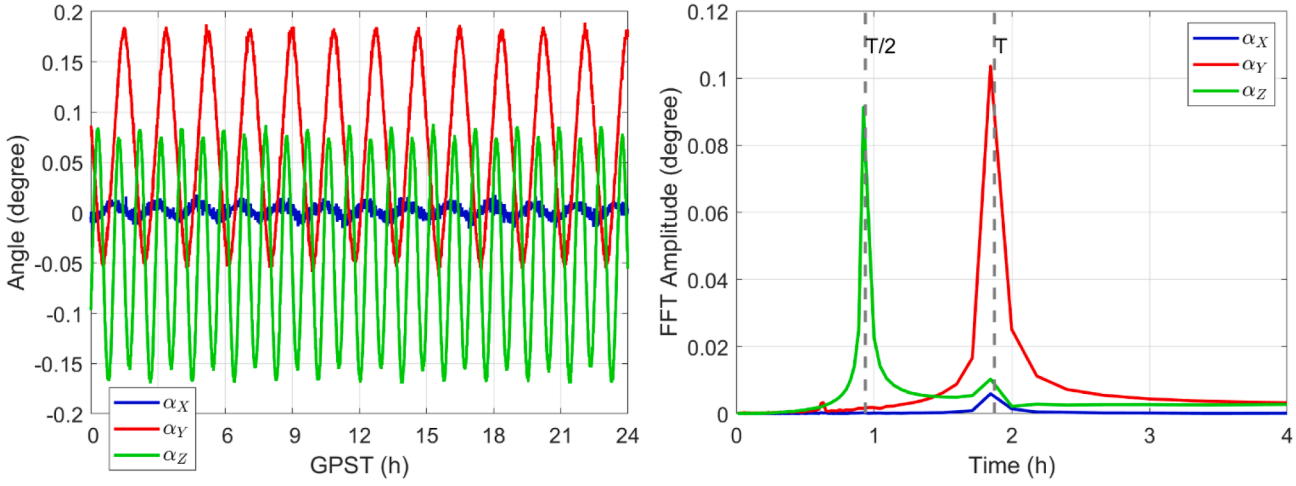

Fig. 2. (Left) Rotation angles between the transformed body-fixed frame and the RTA frame (see Eqs. (7)-(10)) and (right) their FFT for Sentinel-6A on February 1, 2022. "T" in the right panel indicates the orbital period of Sentinel-6A.

Table 3
RMS of the rotation angles and the angle rates between the transformed body-fixed frame and the RTA frame for LEO satellites Sentinel-6A and Sentinel-3B. Note that "6A" and "3B" refer to Sentinel-6A and Sentinel-3B, respectively.

Parameter	α_X		α_Y		α_Z	
	6A	3B	6A	3B	6A	3B
Mean of the angles	0.002°	0.000°	0.064°	0.001°	−0.040°	−0.001°
STD of the angles	0.006°	0.002°	0.078°	0.040°	0.084°	0.111°
RMS of the angles	0.006°	0.002°	0.101°	0.040°	0.093°	0.111°
RMS of the angle rates	0.00015°/s	0.00008°/s	0.00017°/s	0.00013°/s	0.00019°/s	0.00025°/s

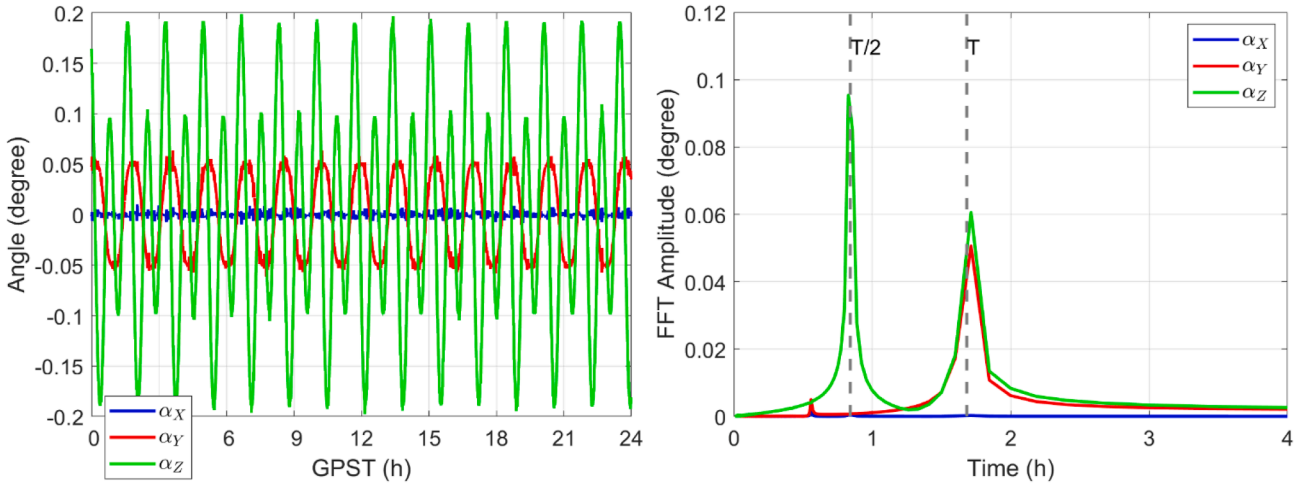

Fig. 3. (Left) Rotation angles between the transformed body-fixed frame and the RTA frame (see Eqs. (7)-(10)) and (right) their FFT for Sentinel-3B on August 15, 2018. "T" in the right panel indicates the orbital period of Sentinel-3B.

Table 4
Simulation scenarios for the rotation angles between the transformed body-fixed frame and the RTA frame.

Scenario	Pattern	Mean of rotation angles (°)	Averaged RMS of rotation angles (°)	Averaged RMS of angle rates (°/s)
A	Trigonometric functions	0.002/ 0.070/ −0.050	0.132	0.00015
B		0.003/ 0.070/ −0.051	0.249	0.00030
C		0.004/ 0.070/ −0.052	0.611	0.00075
D	Random-walk processes	0.067/ 0.206/ −0.066	0.150	0.00033
E		−0.226/ 0.019/ −0.368	0.280	0.00050
F		0.208/ −0.820/ −0.281	0.647	0.00125

$$\alpha_Z = \Delta\alpha_Z + A_S \times \left(\sin\left(\frac{2\pi}{3} + \frac{4\pi}{T} \times t\right) + \sin\left(\frac{2\pi}{3} + \frac{2\pi}{T} \times t\right)\right) \tag{19}$$

where T denotes the orbital period of the LEO satellite. $\Delta\alpha_X$, $\Delta\alpha_Y$ and $\Delta\alpha_Z$ are offsets in the rotation angles α_X, α_Y and α_Z, respectively, which are set to 0.002, 0.07 and −0.05 degrees in the three directions, respectively, for the Scenarios A to C. A_S is the amplitude of the periodic rotation angles, which are set to about 0.15, 0.3, and 0.75 degrees for Scenarios A, B and C, respectively.

For Scenarios D to F, the random-walk rotations are simulated as follows:

$$\alpha_X = \Delta\alpha_X + \text{cumsum}(\sigma_S \times \text{randn}(n_t)) \tag{20}$$

$$\alpha_Y = \Delta\alpha_Y + \text{cumsum}(\sigma_S \times \text{randn}(n_t)) \tag{21}$$

$$\alpha_Z = \Delta\alpha_Z + \text{cumsum}(\sigma_S \times \text{randn}(n_t)) \tag{22}$$

where $\text{randn}(n_t)$ generates a Gaussian white noise with n_t denoting the number of simulated time points. σ_S denotes the standard deviation of the white noise for scenario S, which is set to 3.3×10^{-4}, 5×10^{-4} and 0.0013 degrees for Scenarios D, E and F, respectively. The $\text{cumsum}(\bullet)$ term calculates the accumulated sum of the time series in $(\bullet)$. In addition to the trigonometric functions and random-walk processes, other patterns and noise types could exist in the rotation angles, e.g., white noise. They are worthwhile to study in future research, but they were not attempted in this contribution.

Table 4 gives the statistics of the rotation angles for these different simulation scenarios. Enlarged attitude instabilities are introduced compared to those of the tested Sentinel satellites. The three rotation angles of Scenarios A and D are shown in Fig. 4 for the first 24 h. The very weak attitude control, e.g., that may be used in some CubeSats, are not assumed to be used in navigation LEO satellites, and thus are not discussed in this study.

The rotation angles under different simulation scenarios exhibit different short- to long-term stabilities. The Modified Allan Deviations (MDEVs) of the rotation angle α_Z are illustrated in Fig. 5 under Scenarios A to F. For comparison purposes, the real rotation angle α_Z of Sentinel-3B on August 15, 2023, are also given (see the grey line). Scenarios A to C with periodic patterns show good short-term stabilities, but enlarged MDEVs can be observed at longer averaging times due to the periodic behaviors in the simulations. For Scenarios D to F, the short-term stabilities are worse than those of Scenarios A to C, but the MDEVs are reduced to a lower level

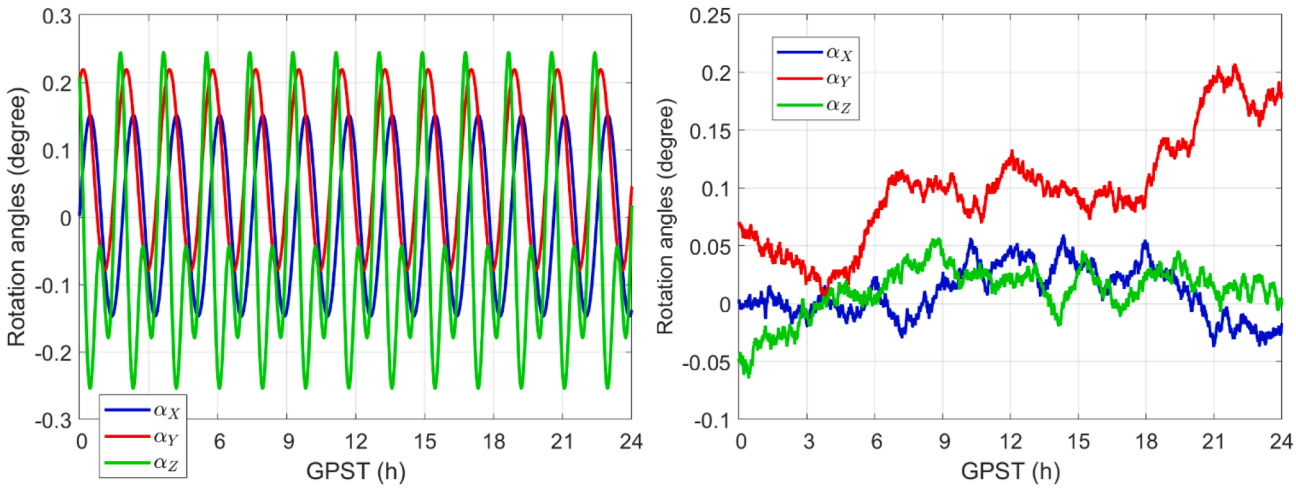

Fig. 4. Rotation angles between the transformed body-fixed frame and the RTA frame for (left) simulation Scenario A and (right) simulation Scenario D (see Table 4) in the first 24 h.

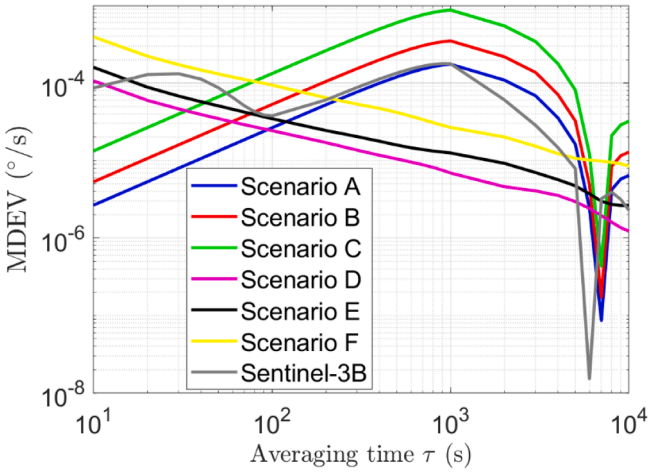

Fig. 5. MDEV of the rotation angle α_Z under different simulation scenarios and for real data of Sentinel-3B on August 15, 2018.

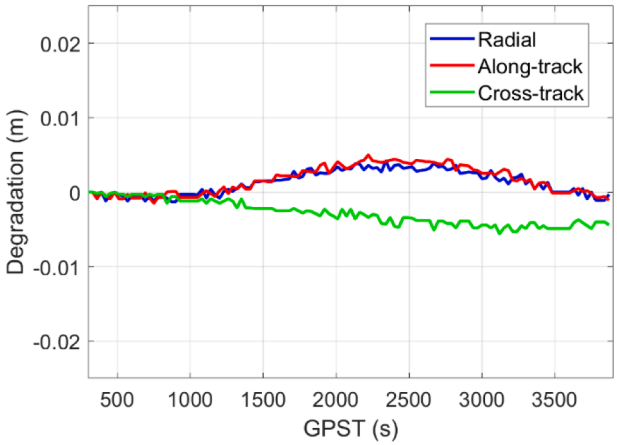

Fig. 6. Degradations in the predicted APC orbits in 1 h prediction interval due to the attitude instability. The real attitudes of Sentinel-6A on February 2, 2022, were used.

at increasing averaging times. From Fig. 5 it can be seen that the periodical variations in Sentinel-3B play a dominant role in its mid- to long-term stabilities. These systematic effects covered other noise types.

3.2.2. *Degradations in the predicted APC orbits*

Based on Section 2, the APC orbits can be determined after constructing the transformation matrix from the body-fixed frame to the ECEF system (R_{B2ECEF}), and when the vector from the CoM to the APC ($\Delta\vec{\gamma}_{\mathrm{LB}}$) is known in the body-fixed frame (see Eq. (14)). The latter term relates to the LEO satellite antenna transmitting navigation signals toward the Earth, which does not exist for the tested Sentinel satellites. For a science-oriented LEO satellite, the antenna sensor offsets (ASO) from the CoM to other antennas are typically at meter level, e.g., the ASO of GNSS antennas at Sentinel-6A. As such, the $\Delta\vec{\gamma}_{\mathrm{LB}}$ is set to (1 m, −0.01 m, 1.2 m) in this study for demonstration purposes. The APC orbits in the prediction period are first determined by correcting the CoM in the prediction interval with the known attitude quaternions, forming the references for comparison with the predicted case later (see Section 2.2). The differences of the estimated APC orbits between these two terms, i.e., with known and predicted attitudes, form the degradations of the predicted APC orbits caused by attitude instability.

Fig. 6 shows the degradations of the Sentinel-6A APC orbits in the 1 h prediction period due to the attitude instability. The prediction interval started at 00:05:00 in GPS Time (GPST) on February 2, 2022. The rotation angles at the prediction starting time were used during the entire prediction interval, which slightly varies from the real rotation angles during this period. As shown in Fig. 6, the attitude instability of Sentinel-6A leads to degradations of a few millimeters. It can be also observed that the degradations do not always increase with the prediction time. In the radial (shown in blue) and along-track (red) directions, the degradations begin to decrease at around the prediction time of 40 min. This could be related to the periodic behaviors of the rotation angles, as depicted in Fig. 2.

The simulation scenarios in Table 4 give more possibilities for studying the APC orbit degradations. Fig. 7 illustrates the APC orbit degradations in the along-track direction for Scenarios A to F, where those of Sentinel-6A are given for comparison (grey line). It can be observed that Scenarios A to C with periodic behaviors generally exhibit larger degradations than those for Scenarios D to F with higher short-term noise. For Scenario C with an RMS of about 0.6 degrees of the rotation angles, the degradation has reached a few cm.

Using the data from February 2 to 8, 2022, with starting time of the 1 h prediction interval shifted from 00:00:00 on February 2, 2022, to 23:55:00 on February 8, 2022, with a step of 5 min, 1728 samples (from February 2 to 7, 2022) were used to evaluate the RMS of the degradations at different prediction times. Fig. 8 shows the OURE of the degradations in the predicted APC orbits caused by the attitude instabilities

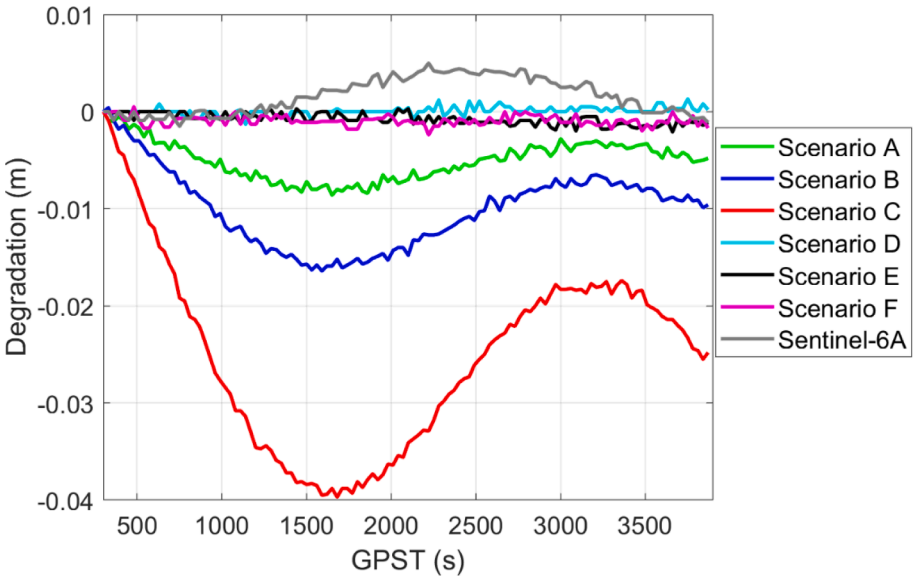

Fig. 7. Degradations in the predicted APC orbits in the along-track directions for Sentinel-6A and for different simulation scenarios in 1 h prediction period due to the attitude instability.

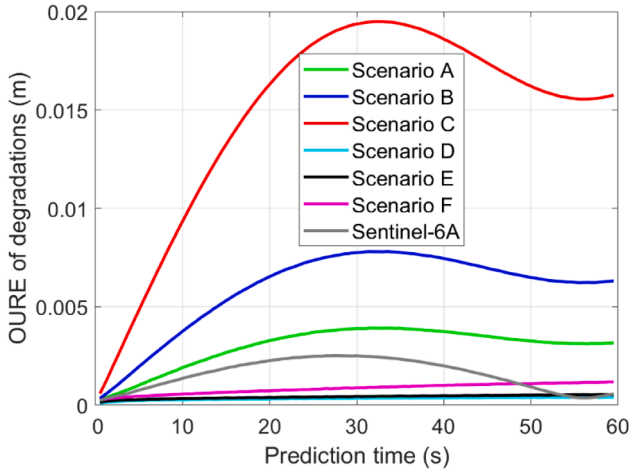

Fig. 8. OURE of the degradations in the predicted APC orbits due to attitude instabilities for Sentinel-6A with different simulation scenarios.

at different prediction times and for different scenarios. The results for Sentinel-6A are also plotted for comparison. It can be observed that Scenarios A to C with increasing periodic patterns lead to relatively large OURE degradations, i.e., nearly 2 cm for Scenario C. However, the degradation does not always increase with the prediction time. This is related to the periodic behaviors of the simulated rotation angles. In contrast, although with relatively large short-term noise, Scenarios D to F, which are based on simulated random-walk rotation angles, exhibit much smaller OURE degradations during the prediction hour, i.e., a few millimeters. However, the OURE increases almost linearly with time. This suggests that the OURE will get larger for a longer prediction time when applying the random-walk scenarios.

The averaged RMS of the degradations in the predicted APC orbits are illustrated in Fig. 9 for Sentinel-6A with different simulation scenarios. Among the three directions, the RMS of the cross-track directions exhibits the largest amplitudes, which is related to the smallest cross-track element in the offset vector from the CoM to the APC as defined at the beginning of this sub-section. The 3D RMS, as shown in Fig. 9, reached 4 cm for Scenario C with a relatively large periodic pattern in the rotation angles (0.6° in 1D on average).

3.3. Ephemeris fitting of the LEO satellite APC orbits

The LEO satellite CoM orbits can be fitted into LEO-specific ephemeris parameters. For proper selection of the ephemeris parameters and a short fitting time, the CoM fitting errors can be limited to a small amplitude, e.g., a few millimeters in the OURE for 18-parameter fitting and a fitting time of 10 min using the Sentinel-3B flying at about 810 km [26].

Compared with the CoM orbits, the motion of the APC orbits is not only influenced by the orbital dynamics, but also the attitude itself. This does not only affect the prediction of the APC orbits as described in Section 3.2 but could also affect the ephemeris fitting, as the ephemeris parameters do not intend to cover the instability of the satellite attitude. In this section, based on the real attitudes of Sentinel-6A and the simulated attitudes in Scenarios C and F, i.e., the two simulation scenarios with the largest attitude instabilities, the errors of the 18-parameter APC ephemeris fitting are studied. The analysis is split into two categories for each type mentioned above, i.e., the APC orbit fitting with known quaternions, and the APC orbit fitting using predicted attitudes (see Eq. (11)). The fitting time is set to 25–35 min in each prediction interval to cover the period with the largest degradation in the APC orbit prediction in Scenario C (see Fig. 8). The start of the fitting time is shifted from 00:25:00 (GPST) on February 2, 2022, to 00:20:00 (GPST) on February 3, 2022, with a step of 5 min. The orbits were fitted using a one-second sampling interval.

The average RMS of the ephemeris fitting are listed in Table 5 for the CoM orbits, the known and predicted APC orbits for Sentinel-6A. Those of the simulation Scenarios C and F are also given for the known and predicted APC orbits. It can be seen that the investigated attitude instabilities have no significant influences on the ephemeris fitting. The 3D RMS of the fitting errors remains almost the same when fitting the APC orbits instead of the CoM orbits. With the short ephemeris fitting interval of 10 min, the ephemeris fitting errors do not vary much for different scenarios as long as corrections from the CoM to the APC are “smooth”. The prediction accuracies themselves do not play a major role. This agrees with the conclusions of Wang et al. [26], where the ephemeris fitting errors for predictions of POD results of different accuracies are very similar. The ephemeris fitting errors are mainly determined by the following factors:

- Length of the fitting interval

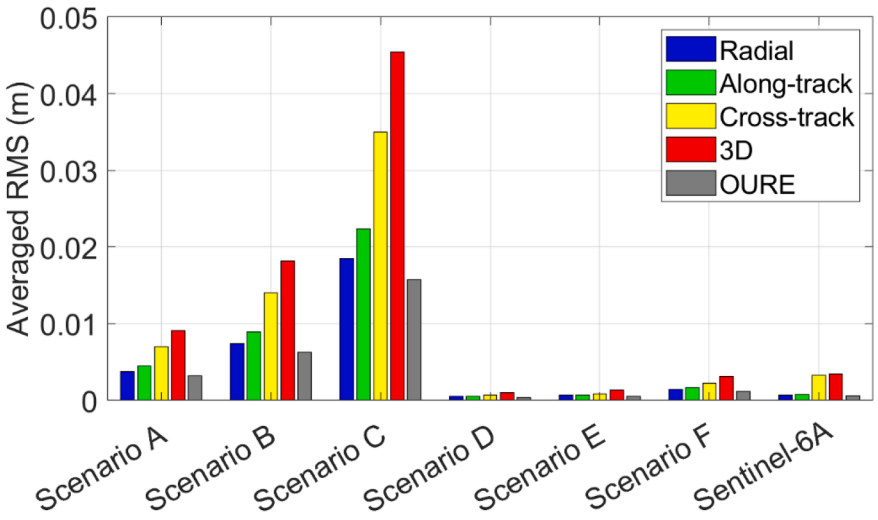

Fig. 9. Averaged RMS in different directions and the OURE degradations in the predicted APC orbits for different simulation scenarios and for Sentinel-6A.

Table 5
Average RMS of the 18-parameter ephemeris fitting errors of the APC orbits under Scenarios C, F, and for Sentinel-6A with known and predicted attitudes. Those for the CoM orbits are given for comparison.

Scenario	σ_R (mm)	σ_T (mm)	σ_A (mm)	σ_{3D} (mm)	σ_{OURE} (mm)
CoM	0.8	3.4	0.5	3.6	2.0
C (known)	0.9	3.4	0.6	3.6	2.0
C (predicted)	0.9	3.4	0.6	3.6	2.0
F (known)	0.9	3.4	0.6	3.6	2.0
F (predicted)	0.9	3.4	0.6	3.6	2.0
Sentinel-6A (known)	0.9	3.5	0.6	3.6	2.0
Sentinel-6A (predicted)	0.9	3.4	0.6	3.6	2.0

- Height of the LEO satellites
- Number of the ephemeris parameters.

As shown in Wang and El-Mowafy [19], for a certain LEO satellite and a certain fitting strategy, the ephemeris fitting errors do not significantly increase with time even for a prediction period of 6 h with a prediction period of a few meters, as long as the prediction strategy is good enough to produce the orbital flow described by the ephemeris parameters.

4. Conclusions and discussions

Nowadays, real-time orbital products of LEO satellites are required at a high accuracy to fulfill the needs of different applications. For navigation purposes, instead of the CoM orbits, users need the orbits at the APC of the antenna transmitting navigation signals toward the Earth. This requires correcting the CoM to the APC orbits in real-time, and for ephemeris fitting, in a short-term prediction period.

With precisely known attitudes of the LEO satellite and precise calibration of the antenna sensor offset and the antenna phase center offset (PCOs), the correction from the CoM to the APC orbits should be of high precision. However, in the prediction interval, the attitude information can only be predicted. Instead of using the default/expected attitude of the satellite, it is possible to predict the attitude in the prediction period based on the latest attitude information, which contains possible offsets in the rotation angles to the default attitudes. Nevertheless, the temporal attitude variation from the default ones, i.e., the attitude instability, would still influence the predicted attitude and the predicted APC orbits. Furthermore, compared with the ephemeris fitting of the CoM orbits influenced only by the orbital dynamics, the fitting of the APC orbits is affected by the satellite attitudes.

In this study, the real attitudes of the LEO satellite Sentinel-6A were used as examples, together with other amplified attitudes simulated with 1/rev and 2/rev periodic functions or random-walk processes. The degradations in the predicted APC orbits caused by attitude instabilities were assessed. For Sentinel-6A, the rotation angles from the real to the default attitude exhibit 1/rev patterns in all three directions, and 2/rev patterns around the Z-axis (nadir direction). The RMS of the rotation angles are around 0.06–0.1 degrees, which results in a few millimeters of degradations (RMS) in the predicted APC orbits within the first prediction hour. For simulation scenarios with similar periodic patterns but enlarged RMS of the rotation angles, up to about 0.6 degrees, the 3D RMS of the degradations has reached 4 cm. For simulated random-walk processes of the rotation angles, without periodic patterns but with larger short-term noise, the degradations are much smaller but increase linearly with time. For the RMS of the random-walk rotation angles at around 0.6 degrees, the 3D RMS of the APC orbit degradations remains about 3 mm at a prediction time of 1 h.

The influences of the attitude instabilities are also studied for the ephemeris fitting of the APC orbits. For 18-parameter ephemeris with a fitting time of 10 min, compared with the CoM orbit fitting, it was shown that the RMS of the degradations in the APC fitting errors remains insignificant for both the real attitudes from Sentinel-6A and the simulated scenarios. The results of this study suggest that for future LEO navigation satellites with proper attitude control, it is applicable to compute precise APC orbits for short-term prediction periods with predicted attitudes. These predicted attitudes can then be fitted into LEO-specific ephemeris parameters without significantly experiencing large fitting errors.

CRediT authorship contribution statement

Kan Wang: Conceptualization, Methodology, Software, Writing – original draft. **Hang Su:** Software. **Ahmed El-Mowafy:** Writing – review & editing. **Xuhai Yang:** Writing – review & editing.

Declaration of competing interest

The authors declare that they have no known competing financial interests or personal relationships that could have appeared to influence the work reported in this paper.

Data availability

Data will be made available on request.

Acknowledgments

This research is funded by the National Time Service Center, Chinese Academy of Sciences (CAS) (No. E167SC14), the National Natural Science Foundation of China (No. 12073034, No. 12203059), the CAS "Light of West China" Program (XAB2021YN25), Shaanxi Province Key R&D Program Project (2022KW-29), and the Australian Research Council—discovery project No. DP 190102444. We would like to acknowledge the support of the international GNSS monitoring and assessment system (iGMAS) at the National Time Service Center, and the National Space Science Data Center, National Science & Technology Infrastructure of China (http://www.nssdc.ac.cn).

References

[1] T.G.R. Reid, A.M. Neish, T. Walter, P.K. Enge, Broadband LEO Constellations for Navigation, Navig. J. Inst. Navig. 65 (2) (2018) 205–220.
[2] K. Wang, A. El-Mowafy, W. Wang, L. Yang, X. Yang, Integrity monitoring of PPP-RTK positioning. Part II: LEO augmentation, Rem. Sens. 14 (7) (2022) 1599, https://doi.org/10.3390/rs14071599.
[3] K. Wang, B. Sun, W. Qin, X. Mi, A. El-Mowafy, X. Yang, A method of real-time long-baseline time transfer based on the PPP-RTK, Adv. Space Res. 71 (3) (2022) 1363–1376, https://doi.org/10.1016/j.asr.2022.10.062.
[4] O. Montenbruck, E. Gill, Around the world in a hundred minutes, in: Satellite Orbits, first ed., Springer, Berlin, Heidelberg, Germany, 2000, pp. 1–13.
[5] Y. Zhang, Z. Li, Z. Wang, R. Li, H. Yuan, The improvement of BDS Observation Geometry with LEO constellations in Orbit Determination, Measurement 177 (2021), 109228, https://doi.org/10.1016/j.measurement.2021.109228.
[6] GPS World Staff, PNT Roundup: Iridium constellation provides low-Earth orbit satnav service. GPS World, January 12, 2017, 2017. <https://www.gpsworld.com/iridium-constellation-provides-low-earth-orbit-satnav-service/#:~:text=Based%20on%20the%20low%2DEarth,buildings%20and%20other%20difficult%20locations> (Accessed on February 12, 2023).
[7] H. Ge, B. Li, M. Ge, N. Zang, L. Nie, Y. Shen, H. Schuh, Initial assessment of precise point positioning with LEO enhanced global navigation satellite systems (LeGNSS), Remote Sens. 10 (7) (2018) 984, https://doi.org/10.3390/rs10070984.
[8] X. Li, F. Ma, X. Li, H. Lv, L. Bian, Z. Jiang, X. Zhang, LEO constellation-augmented multi-GNSS for rapid PPP convergence, J. Geod. 93 (2018) 749–764, https://doi.org/10.1007/s00190-018-1195-2.
[9] T. Reid, S. Banville, B. Chan, K. Gunning, B. Manning, T. Marathe, A. Neish, A. Perkins, A. Sibois, PULSAR: A New Generation of Commercial Satellite Navigation. ION GNSS+ 2022, September 11-15, Denver, Colorado, USA, 2023.
[10] L. Yang The Centispace-1: A LEO Satellite-Based Augmentation System, Bengaluru, India, 2019.
[11] Xinhua, China launches new test satellites via Kuaizhou 1A carrier rocket. China Daily, 2022. Accessed on January 28, 2023 at https://www.chinadaily.com.cn/a/202209/06/WS6316b9eca310fd2b29e76371.html.
[12] L. He, X. He, Y. Huang, Enhanced precise orbit determination of BDS-3 MEO satellites based on ambiguity resolution with B1C/B2a dual-frequency combination, Measurement 205 (2022), 112197, https://doi.org/10.1016/j.measurement.2022.112197.
[13] Y. Peng, X. Dai, Y. Lou, X. Gong, F. Zheng, BDS-2 and BDS-3 combined precise orbit determination with hybrid ambiguity resolution, Measurement 188 (2022), 110593, https://doi.org/10.1016/j.measurement.2021.110593.
[14] T. Zeng, L. Sui, R. Ruan, X. Jia, L. Feng, G. Xiao, GPS triple-frequency undifferenced and uncombined precise orbit determination with the consideration of receiver time-variant bias, Measurement 169 (2021), 108281, https://doi.org/10.1016/j.measurement.2020.108281.
[15] R. Li, Z. Li, N. Wang, C. Tang, H. Ma, Y. Zhang, Z. Wang, J. Wu, Considering inter-receiver pseudorange biases for BDS-2 precise orbit determination, Measurement 177 (2021), 109251, https://doi.org/10.1016/j.measurement.2021.109251.
[16] R. Tu, R. Zhang, L. Fan, J. Han, P. Zhang, X. Wang, J. Hong, J. Liu, X. Lu, Real-time monitoring of the dynamic variation of satellite orbital maneuvers based on BDS observations, Measurement 168 (2021), 108331, https://doi.org/10.1016/j.measurement.2020.108331.
[17] S. Cakaj, B. Kamo, A. Lala, A. Rakipi, The coverage analysis for low earth orbiting satellites at low elevation, Int. J. Adv. Comput. Sci. Appl. 5 (2014) 6, https://doi.org/10.14569/IJACSA.2014.050602.
[18] Z. Yang, H. Liu, C. Qian, B. Shu, L. Zhang, X. Xu, Y. Zhang, Y. Lou, Real-time estimation of low Earth orbit (LEO) satellite clock based on ground tracking stations, Remote Sens. (Basel) 12 (12) (2020) 2050, https://doi.org/10.3390/rs12122050.
[19] K. Wang, A. El-Mowafy, Proposed orbital products for positioning using mega-constellation LEO satellites, Sensors 20 (20) (2020) 5806, https://doi.org/10.3390/s20205806.
[20] K. Wang, X. Yang, A. El-Mowafy, Visibility of LEO satellites under different ground network distributions, in: Proc. ION GNSS+ 2022, Denver, Colorado, USA, September 2022, 2022d, pp. 2478-2491. doi: 10.33012/2022.18391.
[21] Z. Wang, Z. Li, L. Wang, N. Wang, Y. Yang, R. Li, Y. Zhang, A. Liu, H. Yuan, M. Hoque, Comparison of the real-time precise orbit determination for LEO between kinematic and reduced-dynamic modes, Measurement 187 (2022), 110224, https://doi.org/10.1016/j.measurement.2021.110224.
[22] X. Mao, D. Arnold, V. Girardin, A. Villiger, A. Jäggi, Dynamic GPS-based LEO orbit determination with 1 cm precision using the Bernese GNSS Software, Adv. Space Res. 67 (2) (2021) 788–805, https://doi.org/10.1016/j.asr.2020.10.012.
[23] O. Montenbruck, A. Hauschild, Y. Andres, A. von Engeln, C. Marquardt, (Near-) real-time orbit determination for GNSS radio occultation processing, GPS Solut. 17 (2013) 199–209, https://doi.org/10.1007/s10291-012-0271-y.
[24] A. Allahvirdi-Zadeh, K. Wang, A. El-Mowafy, POD of small LEO satellites based on precise real-time MADOCA and SBAS-aided PPP corrections, GPS Solut. 25 (2021) 31, https://doi.org/10.1007/s10291-020-01078-8.
[25] A. Hauschild, J. Tegedor, O. Montenbruck, H. Visser, M. Markgraf, Precise onboard orbit determination for LEO satellites with real-time orbit and clock corrections. Proc. ION GNSS+ 2016, Institute of Navigation, Portland, Oregon, USA, 2016.
[26] K. Wang, J. Liu, H. Su, A. El-Mowafy, X. Yang, Real-time LEO satellite orbits based on batch least-squares orbit determination with short-term orbit prediction, Remote Sens. (Basel) 15 (1) (2023) 133, https://doi.org/10.3390/rs15010133.
[27] X. Li K. Zhang X. Meng W. Zhang Q. Zhang X. Zhang X. Li Precise Orbit Determination for the FY-3C Satellite Using Onboard BDS and GPS Observations from 2013, 2015, and 2017 Engineering 6(8) (2020) 904–912. 10.1016/j.eng.2019.09.001.
[28] O. Montenbruck, S. Hackel, M. Wermuth, F. Zangerl, Sentinel-6A precise orbit determination using a combined GPS/Galileo receiver, J. Geodesy. 95 (9) (2021) 109, https://doi.org/10.1007/s00190-021-01563-z.
[29] X. Gong, W. Zhang, Q. Wang, F. Wang, X. Li, J. Sang, W. Liu, Precise real-time navigation of the small TJU-1 satellite using GPS, GLONASS and BDS. Meas. 204 (2022), 112090, https://doi.org/10.1016/j.measurement.2022.112090.
[30] O. Montenbruck, F. Kunzi, A. Hauschild, Performance assessment of GNSS–based real–time navigation for the Sentinel-6 spacecraft, GPS Solutions 26 (2021b) 12. doi: 10.1007/s10291-021-01198-9.
[31] A. Hauschild, O. Montenbruck, P. Steigenberger, I. Martini, I. Fernandez-Hernandez, Orbit determination of Sentinel-6A using the Galileo high accuracy service test signal, GPS Solut. 26 (2022) 120, https://doi.org/10.1007/s10291-022-01312-5.
[32] X. Jia, T. Lv, F. He, H. Huang, Collaborative data downloading by using inter-satellite links in LEO satellite networks, IEEE Trans. Wirel. Commun. 16 (3) (2017) 1523–1532, https://doi.org/10.1109/TWC.2017.2647805.
[33] K. Wang, A. El-Mowafy, X. Yang, URE and URA for predicted LEO satellite orbits at different altitudes, Adv. Space Res. 70 (8) (2022) 2412–2423, https://doi.org/10.1016/j.asr.2022.08.039.
[34] K. Wang, A. El-Mowafy, H. Su, X. Yang, On the very short and very long LEO satellite orbit prediction, Long Beach, CA, USA, 2023, pp. 725–735 10.33012/2023.18665.
[35] GPS ICD, GPS Interface Specifications IS-GPS-200, Revision M, NAVSTAR GPS Space Segment/Navigation User Interfaces, 2021. <https://www.gps.gov/technical/icwg/IS-GPS-200M.pdf> May 2021 Accessed on June 13, 2023 at.
[36] L. Carlin, A. Hauschild, O. Montenbruck, Precise point positioning with GPS and Galileo broadcast ephemeris parameters, GPS Solut. 25 (2021) 77, https://doi.org/10.1007/s10291-021-01111-4.
[37] K. Shoemakef, Animating rotation with quaternion curves, San Francisco, USA, 1985, pp. 245–254.
[38] X. Xie, T. Geng, Q. Zhao, X. Liu, Q. Zhang, Liu J (2018) Design and validation of broadcast ephemeris for low Earth orbit satellites, GPS Solut. 22 (2018) 54, https://doi.org/10.1007/s10291-018-0719-9.
[39] CPOD, Copernicus POD regular service review Apr.–Jun 2021, copernicus Sentinel-1, -2, -3 and -6 precise orbit determination service (CPOD). GMV-CPOD-RSR-0021, 2021, 2021/06/23.
[40] R. Dach S. Lutz P. Walser P. Fridez Bernese GNSS software version 5.2. User manual, Astronomical Institute 2015 University of Bern, Bern Open Publishing 10.7892/boris.72297.
[41] L. Chen, W. Jiao, X. Huang, C. Geng, L. Ai, L. Lu, Z. Hu, Study on signal-in-space errors calculation method and statistical characterization of BeiDou navigation satellite system, in: J. Sun, W. Jiao, H. Wu, C. Shi, Proceedings of the China Satellite Navigation Conference (CSNC), Lecture Notes in Electrical Engineering, vol. 243, Springer, Berlin, Heidelberg, Germany, 2013.